

Supramolecular Halogen Bond Passivation of Organic–Inorganic Halide Perovskite Solar Cells

Antonio Abate,[†] Michael Saliba,[†] Derek J. Hollman,[†] Samuel D. Stranks,[†] Konrad Wojciechowski,[†] Roberto Avolio,[‡] Giulia Grancini,[§] Annamaria Petrozzi,[§] and Henry J. Snaith*,[†]

[†]Clarendon Laboratory, Department of Physics, University of Oxford, Parks Road, Oxford OX1 3PU, United Kingdom

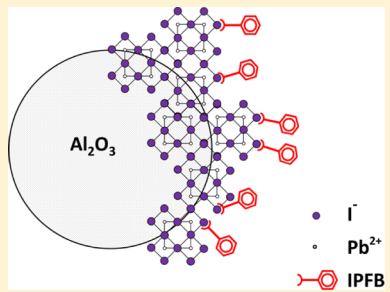
[‡]Institute of Polymer Chemistry and Technology (ICTP), National Research Council of Italy, Via Campi Flegrei 34, 80078 Pozzuoli (NA), Italy

[§]Center for Nano Science and Technology@PoliMi, Istituto Italiano di Tecnologia, Via Pascoli 70/3, 20133 Milano, Italy

Supporting Information

ABSTRACT: Organic–inorganic halide perovskites, such as $\text{CH}_3\text{NH}_3\text{PbX}_3$ ($\text{X} = \text{I}^-$, Br^- , Cl^-), are attracting growing interest to prepare low-cost solar cells that are capable of converting sunlight to electricity at the highest efficiencies. Despite negligible effort on enhancing materials' purity or passivation of surfaces, high efficiencies have already been achieved. Here, we show that trap states at the perovskite surface generate charge accumulation and consequent recombination losses in working solar cells. We identify that undercoordinated iodine ions within the perovskite structure are responsible and make use of supramolecular halogen bond complexation to successfully passivate these sites. Following this strategy, we demonstrate solar cells with maximum power conversion efficiency of 15.7% and stable power output over 15% under constant 0.81 V forward bias in simulated full sunlight. The surface passivation introduces an important direction for future progress in perovskite solar cells.

KEYWORDS: Perovskite, halogen bonding, organic–inorganic halide perovskite, fluorinated materials, solar cells, photovoltaic, perovskite solar cells, surface passivation



Photovoltaic (PV) cells, capable of converting sunlight directly into electricity, are one possible solution to satisfy the global energy demand.¹ When the first crystalline silicon (c-Si) PV devices were demonstrated in 1954, the envisaged manufacturing costs made this technology impractical for large-scale power generation.² Hereafter, exploiting new materials and fabrication procedures has attracted a growing effort to realize a fundamentally lower cost photovoltaic technology. In particular, the recent emergence of organic–inorganic halide perovskite-based solar cells promises to deliver one of the lowest cost technologies that is capable of converting sunlight to electricity at the highest efficiencies.^{3–6} The most promising perovskites used in solar cells to date are organic–inorganic halide compounds with the chemical formula $\text{CH}_3\text{NH}_3\text{PbX}_3$ ($\text{X} = \text{I}^-$, Br^- , Cl^-). They have been used in mesoscopic solar cells as sensitizers; evolving from dye-sensitized solar cells (DSSCs),^{7,8} the dye is replaced by perovskite crystals dispersed on the surface of a mesoporous layer of n-type TiO_2 nanoparticles.^{4,9,10} In the perovskite-sensitized solar cells (PSSCs), the perovskite has to absorb light and then transfer charge across a nanoscale heterojunction to positive (p) and negative (n) type charge collection materials, which are responsible for long-range transport. Unexpectedly, replacing the mesoporous n-type TiO_2 electron conductor with a mesoporous insulating scaffold of Al_2O_3 enhanced the performance of the solar cells since the perovskite absorber was found

to be capable of supporting long-range charge transport itself in addition to being a robust light absorber.^{5,11–14} This Al_2O_3 -based “meso-superstructured solar cell” (MSSC) has further evolved with the significant thinning of the mesoporous Al_2O_3 scaffold to such an extent that within the most efficient devices there exists a solid capping layer of perovskite absorber, and a planar heterojunction between the p-type hole conductor and the perovskite film, similar to a p-i-n heterojunction solar cell (see Figure 1a).^{14–21} In comparison to c-Si and other crystalline semiconductors, where minimizing impurities and crystal imperfections are critical to prepare the highest efficiency PV cells,²² the presence and role of defect sites in the perovskite material have thus far been ignored.^{9,17,23}

Here, we demonstrate that undercoordinated halide ions upon the surface of the organic–inorganic halide perovskite crystals are reducing the cell performance via trapping positive charge at the perovskite p-type hole-conductor heterojunction. We employ supramolecular halogen bonding donor–acceptor complexation to coat the perovskite crystal with iodopentafluorobenzene (IPFB), which passivate these surface hole trapping states. The ensuing solution processed perovskite MSSCs exhibit maximum power conversion efficiency of 15.7%

Received: February 17, 2014

Revised: April 30, 2014

Published: May 1, 2014

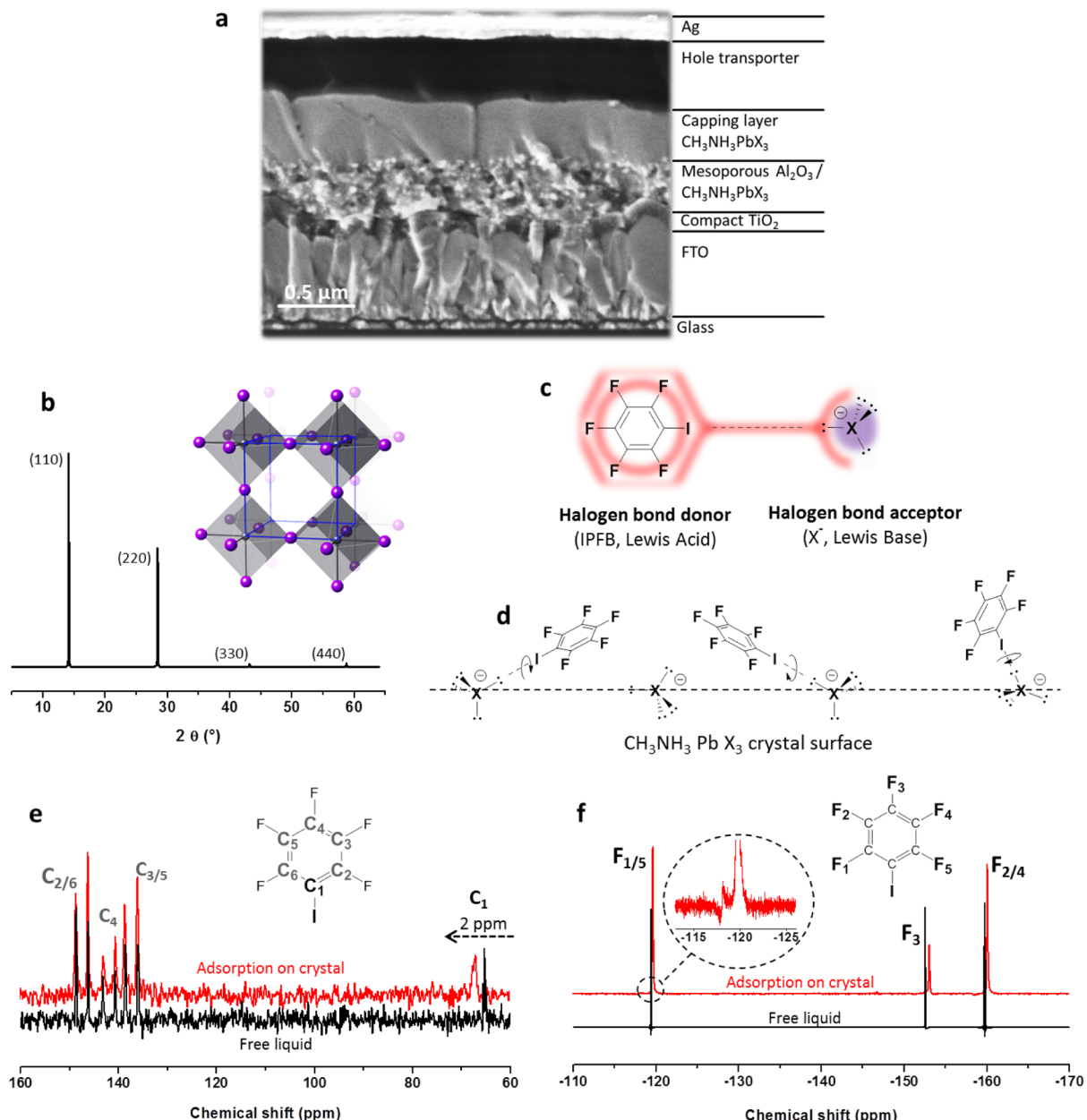


Figure 1. Organic–inorganic halide perovskite crystals coated with monomolecular IPFB layer via halogen bond. (a) Cross-sectional scanning electron microscopy of a complete MSSC. (b) Powder X-ray diffraction pattern (peaks at 2θ angles of 14.1°, 28.4°, 43.1°, and 58.7°; $h\bar{h}0$, $h = 1–4$) and crystal structure of $\text{CH}_3\text{NH}_3\text{PbX}_3$ and its tetragonal crystal unit cell with lattice parameters $a = b = 8.86 \text{ \AA}$ and $c = 12.60 \text{ \AA}$ (Pb, small blue spheres; X, larger purple spheres; CH_3NH_3^+ not shown).²⁴ (c) Schematic view of the halogen bond interaction between the iodopentafluorobenzene (IPFB, halogen bond donor) and a generic halogen anion ($X^- = \text{I}^-, \text{Br}^-, \text{Cl}^-$, halogen bond acceptor) with sp^3 -hybridized valence electrons.²⁷ (d) Schematic view of the IPFB assembly on the crystal surface. (e, f) Solid-state ^{13}C and ^{19}F NMR spectra for IPFB as a liquid and when adsorbed onto the perovskite surface. Inset in (f): zoom-in at -120 ppm.

and stable power output of 15% under constant 0.81 V forward bias in simulated full sunlight.

Results and Discussion. We prepared a mixed halide perovskite of form $\text{CH}_3\text{NH}_3\text{PbX}_3$ ($X^- = \text{I}^-, \text{Cl}^-$) from a solution of methylammonium iodide and lead chloride in dimethylformamide, as previously reported.^{5,15} Figure 1b shows X-ray diffraction peaks at 2θ angles of 14.1°, 28.4°, 43.1°, and 58.7°. A similar diffraction pattern was observed previously for both triiodide and mixed-halide crystals.^{24,25} This pattern matches with an tetragonal perovskite crystal structure, which is the most stable phase at room temperature.²⁶ As visualized in the inset of Figure 1b, in this crystal structure, 6-fold-

coordinated Pb^{2+} cations occupy the corners of the unit cell, surrounded by an octahedron of X^- anions, with CH_3NH_3^+ cations filling the space in the middle of the unit cell.

In these perovskite materials, as well as for most ionic crystals, the coordination number for ions at the crystal surfaces is always lower than in the bulk material. The consequent nonstoichiometric material is comprised of a local excess of positive or negative ions, depending on the Miller index of the exposed surface. Such polar surfaces are known to be unstable, and their apparent natural occurrence has been associated with adsorption of foreign atoms, including oxygen and hydrogen from the air moisture, which passivate the crystal surface by

balancing the local excess charge.^{28–30} For the particular case of $\text{CH}_3\text{NH}_3\text{PbX}_3$ crystals, undercoordinated metal cations at the crystal surface would be unstable to oxygen and water and will form lead oxide and hydroxide species when exposed to air.^{31,32} Similarly, undercoordinated organic cations at the crystal surface are expected to bind with water molecules via hydrogen bridges, which causes hydration of the crystal surface.³³ Conversely, halide anions in crystalline materials have been reported to be relatively stable to air exposure.²⁷ Therefore, while we would not expect to find many “free” Pb^{2+} and CH_3NH_3^+ when the devices are processed in air (as is the case here), it is likely that an excess of undercoordinated X^- ions is present at the crystal surface.

Halide anions (X^-), in particular iodide, can strongly interact with halogenated organic compounds via a specific supramolecular interaction referred to as halogen bonding.^{34,35} This interaction defines any noncovalent bond which involves halogens as an electrophile (Lewis acid, halogen bond donor).³⁶ One of the strongest reported halogen bond donors is iodopentafluorobenzene (IPFB, Figure 1c).^{37,38} In this compound, the highly electronegative fluorine atoms inductively withdraw electron density out of the aromatic ring, which in turn withdraws electron density from the iodine bonded to the aromatic ring ($-\text{C}-\text{I}$), leaving a partial positive charge on this halogen.³⁸ Furthermore, the charge density on the iodine in IPFB is anisotropically distributed, with positive electrostatic potential localized opposite the carbon on the extension of the $-\text{C}-\text{I}$ bond axis. This electropositive region can interact attractively with any electron-rich sites, and the interaction is especially strong with halogen anions (X^- , Lewis base, Figure 1c).²⁷ Since this positive region on the iodine is surrounded by a belt of negative electrostatic potential,³⁸ any shift from a coaxial arrangement of $-\text{C}-\text{I}\cdots\text{X}^-$ (see Figure 1c) results in electrostatic repulsions. Thus, the angle $-\text{C}-\text{I}\cdots\text{X}^-$ is always close to 180° , whereas the $\text{I}\cdots\text{X}^-$ distance depends on the particular structure.³⁹

We utilize halogen bonding to self-assemble IPFB on the surface of $\text{CH}_3\text{NH}_3\text{PbX}_3$ (see Figure 1d), with the overall purpose to passivate the exposed, undercoordinated halogen anions. To demonstrate the presence of adsorbed IPFB and the nature of the interaction with the $\text{CH}_3\text{NH}_3\text{PbX}_3$ crystal surface, we performed solid state ^{13}C and ^{19}F nuclear magnetic resonance (NMR) measurements. Figure 1e shows the chemical shift of ^{13}C NMR for neat IPFB, which is liquid at room temperature, and for IPFB adsorbed on the perovskite surface. No significant shift was found for the fluorine-bound carbons (C_{2-6}) in the range 135–150 ppm, while the signal of the iodine-bearing carbon (C_1) shifted 2 ppm downfield. This trend in the chemical shift of the carbons is analogous to what is reported in similar compounds involved in halogen bonding, both in solution⁴⁰ and in solid crystals.⁴¹ Significant changes in carbon chemical shift have also been described for fluorinated benzyl rings adsorbed via π -interactions on polar surfaces.⁴² However, this occurrence can be ruled out since its effect on ^{13}C chemical shift is in the opposite direction to the shift we observe here (see Supporting Information for additional experiments).⁴⁰ Thus, ^{13}C NMR gives strong evidence that IPFB is adsorbed via halogen bonding to the $\text{CH}_3\text{NH}_3\text{PbX}_3$ crystal surface, as schematically illustrated in Figure 1d.

Figure 1f shows ^{19}F NMR collected on the same samples, which allows the extraction of more detailed information than ^{13}C NMR.⁴² The ^{19}F IPFB signals recorded on the treated perovskite are made of two components (inset Figure 1f): one

small component at the same frequency as liquid IPFB and one much more intensely shifted by about 0.5 ppm upfield. This supports the conclusion that the IPFB molecules are adsorbed onto the crystal surface and most of the unadsorbed excess is removed (see Supporting Information for additional details).

We prepared perovskite MSSCs by a slightly adapted method to that previously reported in the literature,¹⁵ using 2,2',7,7'-tetrakis(*N,N*-di-*p*-methoxyphenylamine)9,9'-spirobifluorene (Spiro-OMeTAD) as the organic hole transporter. In contrast to previous reports, we coated the perovskite precursor solution onto a warmed substrate (70°C), which results in thicker perovskite films and higher photocurrents. Detailed performance variations with substrate temperature are shown in Supporting Information Figure S2. In Figure 2 we show the

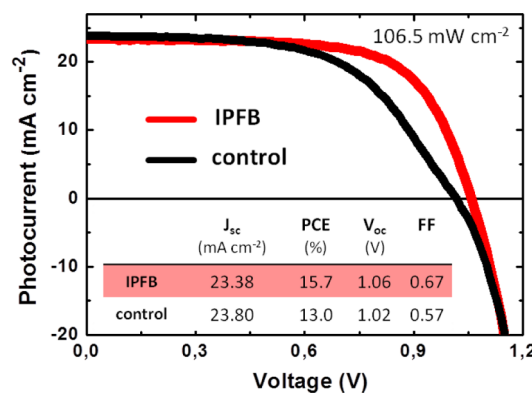


Figure 2. Perovskite solar cells with and without IPFB treatment. J – V curves and performance parameters (table inset) of the best perovskite MSSCs, with and without the IPFB treatment, using Spiro-OMeTAD as hole transporter; devices were measured under AM1.5 simulated sunlight of 106.5 mW cm^{-2} equivalent solar irradiance using shadow masking to define the active area.⁴³

J – V characteristics of the best performing perovskite MSSCs with and without IPFB treatment. The untreated device already delivers a substantial power conversion efficiency (PCE).^{5,15} Upon IPFB treatment, the short-circuit current density (J_{sc}) and the open-circuit voltage (V_{oc}) remain similar, while the fill factor (FF) is dramatically improved. The table inset in Figure 2 shows that the maximum PCE increases from 13.0% to over 15.7%, representing a step improvement for the MSSCs (see Supporting Information for statistical analysis). In addition, for the IPFB-treated device we observed PCE stabilize above 15% under a fixed 0.81 V forward bias (voltage at maximum power output derived from J – V curve, see Supporting Information Figure S15). A complete comparison between the current–voltage scan derived PCE and the stabilized power output for cells with and without IPFB treatment is given in Supporting Information Figure S14.

We note that the control device exhibits a slight bend in the J – V curve near 0.9 V (see Figure 2a), which is responsible for the relatively poor fill factor. Similarly shaped J – V curves have previously been reported in several works for both organic and inorganic solar cells, and it is been generally referred to as an “S-shaped” J – V curve.^{44,45} The origin of the S-shape has been attributed to an energetic barrier for charge extraction, which may occur at any interface in the device. Often the interface between the p-type component and the electrode has been found to be responsible. Few studies so far have focused on the interface between the n- and p-type components. Particularly,

Canesi and co-workers reported that built-in dipoles at a p–n interface for hybrid organic–inorganic devices may create an energetic barrier for charge extraction, which results in S-shaped J – V curves.⁴⁶ If the inorganic components are ionic crystals, such as the perovskites used in this work, then native dipoles would occur at the organic–inorganic interface, between the hole transporter and the perovskite. Indeed, the presence of undercoordinated halides at the crystal surface gives rise to local excess of negative electrostatic charge, which may trap the holes injected into the Spiro-OMeTAD, generating interfacial dipoles. The IPFB treatment could effectively screen the electrostatic charge of the halides exposed at the crystal surface and prevent dipole formation. Though the S-shape is often unclear, devices without the IPFB passivation treatment systematically exhibit worse fill factor as shown in Supporting Information Figure S3.

To elucidate the dynamics of charge transfer and recombination occurring at the perovskite/hole transporter interface, we performed transient absorption (TA) measurements in the femtosecond–microsecond time window on perovskite films formed on a mesoporous Al_2O_3 scaffold deposited on glass and coated with Spiro-OMeTAD, with and without the IPFB treatment.⁴⁷ In Figure 3a, we show the TA femtosecond spectra in the near-infrared, covering the 850–1150 nm spectral region, and the TA dynamics at 1100 nm. The control sample with no IPFB treatment shows a flat negative band (photoinduced absorption, PA) at 200 fs, which

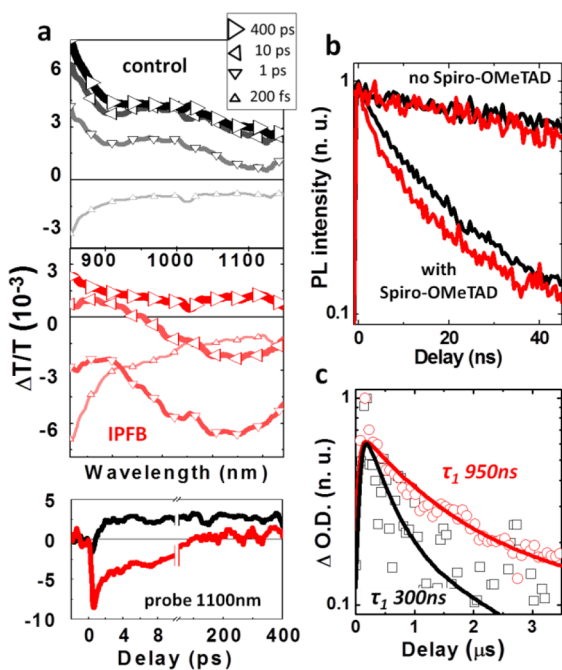


Figure 3. Perovskite/hole transporter interface charge dynamics. Red and black lines indicate samples with and without the IPFB treatment, respectively. (a) Ultrafast transient absorption spectra and dynamics at 1100 nm of perovskite films formed on a mesoporous Al_2O_3 scaffold deposited on glass and coated with Spiro-OMeTAD; excitation at 500 nm (14 $\mu\text{J}/\text{cm}^2/\text{pulse}$). (b) Time-resolved photoluminescence quenching, probing the emission from samples with and without Spiro-OMeTAD, with excitation at 510 nm (0.03 $\mu\text{J}/\text{cm}^2/\text{pulse}$). (c) Nanosecond transient absorption dynamics for the IPFB treated (circles) and untreated (squares) samples; excitation at 500 nm (100 $\mu\text{J}/\text{cm}^2/\text{pulse}$), probe at 640 nm. The continuous lines represent the double-exponential fitting with the shorter lifetimes (τ_1) reported.

is quickly overtaken by the formation of a broad positive band (photobleaching, PB) on the subpicosecond time scale. We also observed similar PB band on perovskite films coated with an insulating organic layer (no hole transporter) in quasi-steady-state photoinduced absorption,⁴⁶ which is shown in Supporting Information Figure S6. Since its spectral position is distinct from the photoluminescence and the linear absorption spectral region, we tentatively assign these features to bleaching of sub-band-gap absorption. For similar perovskite/hole transporter film, photothermal deflection spectroscopy also detects sub-band-gap absorptions in the same spectral region, but this will be looked at in more detail in ongoing work. We note that our assignment to the species here is different than that of Marchioro and co-workers, who assign the TA signal at 1400 nm to the free carriers in the perovskite.⁴⁸ However, since no spectra are shown by Marchioro and co-workers, we cannot critically judge their assignments. For the device samples with the IPFB treatment, the TA evolution is considerably different. We continue to observe the PA at 200 fs; however, it evolves into a different PA band before we are able to observe PB on the picosecond time scale. This new PA band, which is clearly evident in the 1 ps trace, extends further in the near-infrared and is coincident with the absorption of the positive charge on Spiro-OMeTAD (see Supporting Information Figure S6).⁴⁹ The PA band still competes with the formation of the broad PB band observed without the IPFB, which overbears the PA on the picosecond time scale. This trend indicates that the surface treatment makes the hole transfer process to the Spiro-OMeTAD dominate on subpicosecond time scale. Disentangling all the TA features is challenging; however, the results above are consistent with an efficient hole transfer to the Spiro-OMeTAD when the perovskite film is treated with IPFB. To probe a signature of hole transfer from the perovskite to the Spiro-OMeTAD, we have in addition performed a transient photoluminescence quenching experiment. In Figure 3b, we show that the Spiro-OMeTAD quenches the photoluminescence of the perovskite marginally faster with the IPFB treatment.

To probe the charge recombination dynamics at the perovskite/hole transporter interface, we measured the decay of the TA signal for the oxidized Spiro-OMeTAD species in the nano-to-millisecond time scale.⁴⁹ In Figure 3c we show the TA dynamics probed at 640 nm from samples with and without the IPFB treatment. In the untreated sample, the holes recombine with an initial time constant of approximately 300 ns. In contrast, the IPFB treated sample shows a much longer decay with an initial time constant of approximately 900 ns. Thus, the hole lifetime is approximately 3 times longer, indicating that the Spiro-OMeTAD hole recombination is significantly suppressed with the presence of IPFB.

In order to understand the origin of such slower recombination with the presence of IPFB, we used small perturbation photocurrent and photovoltage decay measurements.⁵⁰ Since the charge collection (or extraction) lifetime in MSSC devices is close to the instrument resolution of our apparatus, we constructed perovskite-sensitized solar cells (PSSCs) replacing thin (300 nm) Al_2O_3 with thick (1.5 μm) mesoporous TiO_2 . In the PSSC configuration, we can moderate the charge transport, forcing the electron transport to be exclusively through the TiO_2 by making thick mesoporous TiO_2 films,^{21,51} with a relatively low coating density of perovskite absorber, but we still observe similar or even greater enhancements in solar cell performance with the IPFB

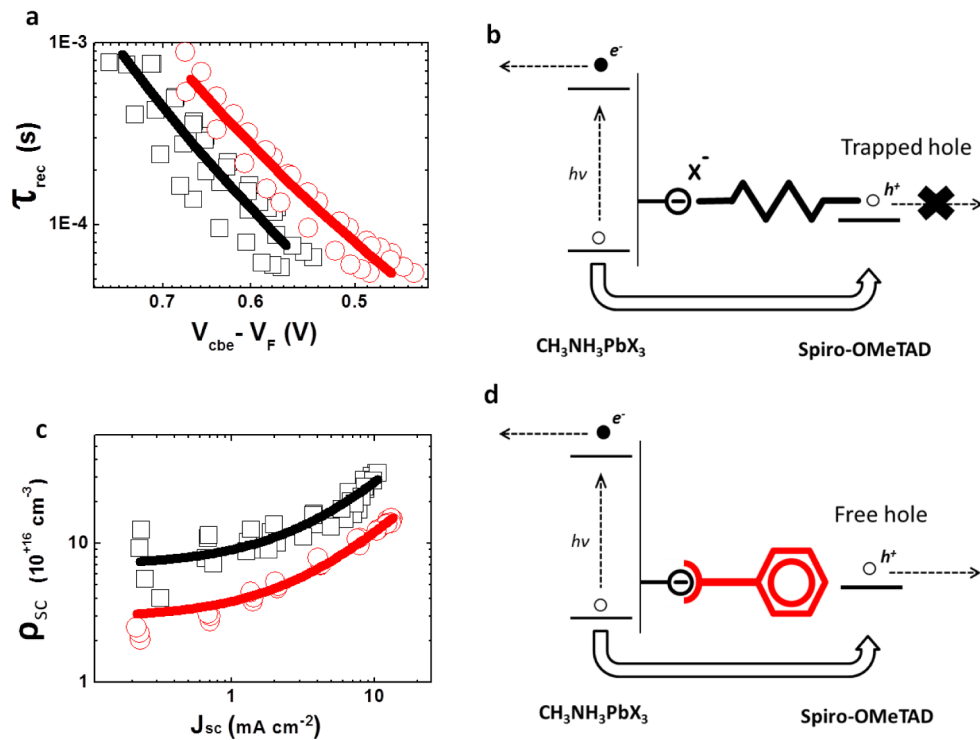


Figure 4. Charge accumulation at the perovskite/hole transporter heterojunction. Red and black lines indicate samples with and without the IPFB, respectively. Photocurrent and photovoltage decay measurements for IPFB-treated and untreated perovskite-sensitized solar cells (PSSCs), as extracted from eight separate devices. (a) Recombination lifetimes (τ_{rec}) against the relative position of the electron quasi-Fermi level with respect to the conduction band edge in the TiO_2 ($V_{\text{cbe}} - V_F$).⁵⁰ In Figure 4a, we show that the IPFB treatment reduces the recombination rate constant ($1/\tau_{\text{rec}}$) by a factor of 3, consistent with the TA results presented in Figure 3d.

treatment (see Supporting Information Figures S7 and S8 for more details). We can probe the relative change in charge recombination at perovskite/hole transporter interface in working devices by plotting the recombination lifetimes (τ_{rec}) against the relative position of the electron quasi-Fermi level with respect to the conduction band edge in the TiO_2 ($V_{\text{cbe}} - V_F$).⁵⁰ In Figure 4a, we show that the IPFB treatment reduces the recombination rate constant ($1/\tau_{\text{rec}}$) by a factor of 3, consistent with the TA results presented in Figure 3d.

Although the inhibition of recombination could explain the improved fill factor we observed with the IPFB treatment, it does not clarify the occasional occurrence of the S-shaped $J-V$ curve. As illustrated in Figure 4b, undercoordinated halides (X^-) at the crystal surface could act as trap sites for the holes on Spiro-OMeTAD. If this is the case, then holes should accumulate at this heterojunction until they have electrostatically screened all of the undercoordinated halides. Therefore, we would expect to see additional buildup of positive charge in the nontreated device. We can directly estimate the relative concentration of this accumulated charge by comparing the total charge extracted under the short-circuit condition (ρ_{sc}) at the same J_{sc} for the devices with and without IPFB treatment.⁵⁰ In Figure 4c, we show that, for any given J_{sc} , there is a much larger background density of charge within the devices without the IPFB treatment. This is consistent with IPFB effectively passivating the undercoordinated halides and reducing the density of accumulated charge at the heterojunction, as illustrated in Figure 4d. Remarkably, the additional background charge density in the control devices is significantly larger than the total charge density in the IPFB treated device. This is consistent with the recent observations by Bisquert and co-

workers¹⁰ and could explain the origin of the unexpectedly large charge accumulation in perovskite solar cells. We hence propose that the S-shaped $J-V$ curve or the relatively low fill factor arises from hole accumulation in the Spiro-OMeTAD at the perovskite/hole transporter heterojunction, which results in a local electric field causing hole drift within the Spiro-OMeTAD toward, rather than away from, the heterojunction. The effect of this electric field may be negligible in short-circuit conditions, but it becomes significant under working conditions with external applied forward bias.⁴⁴

Conclusion. We have introduced a surface passivation method for organic–inorganic halide perovskite solar cells by assembling IPFB via supramolecular halogen bonding. The best PCE of the IPFB-treated MSSCs increased from 13.0% to over 15%, and we elucidated the mechanism responsible for the enhancements: without treatment, undercoordinated halide anions act as hole traps, leading to a significant accumulation of charge at the perovskite/hole transporter heterojunction. This leads to faster recombination and is likely to result in a disadvantageous charge density profile within the hole transporter and perovskite film, which should inhibit fast and efficient charge extraction under working conditions. The IPFB binds to and screens the electrostatic charge from the undercoordinated halide ions, resolving the issue. Notably, for the IPFB-treated device we observed stabilized PCE above 15% under constant 0.81 V forward bias. Beyond advancing the current technology, our work demonstrates that chemical treatments of the perovskite crystal surface can lead to enhanced operation in the solar cells. We expect further improvements in both performance and reproducibility by pacifying any undercoordinated organic and metal cations (A

and B ions in the general formula ABX_3), without relying on atmospheric oxygen and water. Furthermore, careful consideration of the heterojunction between the n-type collection layer and the perovskite must be made to ensure similar losses, specifically with electrons trapped at undercoordinated cations, are not occurring.

Methods. NMR Measurements and Samples Preparation. ^{13}C and ^{19}F NMR spectra were recorded on a Bruker Avance II 400 spectrometer equipped with a double resonance 4 mm MAS probe. For liquid materials as iodopentafluorobenzene (IPFB, Chemical Abstract Services Number 827-15-6), a droplet of the sample was enclosed on a zirconia rotor designed for liquids, with a reduced volume and Kel-F spacer with screw cap to avoid leakage of the sample during spinning. Spinning speed was set to 3 kHz. ^{13}C and ^{19}F chemical shifts were referenced to external secondary standard, adamantane and PTFE, respectively.^{42,52} For the IPFB adsorbed on $\text{CH}_3\text{NH}_3\text{PbX}_3$ crystals, 1 mL of aluminum oxide nanoparticles suspension, (Aldrich, <50 nm particle size, 20 wt % in isopropanol) was placed in a 10 cm diameter Petri dish, and the solvent slowly evaporated on a hot plate to achieve a uniform particles film on the bottom. Then, the Petri dish was heated up to 250 °C to completely remove the solvent and any residue of water from the aluminum oxide. After cooling to 70 °C, the particles film was completely embedded in 4 mL of $\text{CH}_3\text{NH}_3\text{PbX}_3$ precursor, 40 wt % of methylammonium iodide ($\text{CH}_3\text{NH}_3\text{I}$) and lead(II) chloride (PbCl_2), 3:1 molar ratio in dimethylformamide, which has been prepared according to a previously published method.^{5,15} Then, the hot plate temperature was raised to 120 °C for a few minutes to reduce the volume of the liquid phase. After the liquid phase was completely removed, the residual solid was further heated for 1 h at 100 °C. The solid started to turn dark a few minutes after the liquid was completely removed. To achieve a more uniform color distribution, the powder was frequently mixed with a spatula. Then, 5 mL of pure IPFB was added in the Petri at 100 °C and mixed for a few minutes with the solid particles using a spatula. Finally, a uniform black solid was filtered to remove the excess of liquid IPFB and dried under vacuum overnight. To collect the NMR for this sample, a regular 4 mm rotor was used, with spinning speed of 5 kHz.

Optical Characterization. Absorption measurements were carried out on a PerkinElmer Lambda 1050 UV-vis-NIR spectrophotometer (spectra reported in Supporting Information Figure 1S). Steady-state and time-resolved PL measurements were acquired using a time-correlated single photon counting (TCSPC) setup (FluoTime 300, PicoQuant GmbH). Film samples were photoexcited using a 507 nm laser head (LDH-P-C-510, PicoQuant GmbH) pulsed at a frequency of 4.5 MHz, with a pulse duration of 117 ps and fluence of ~30 nJ/cm². The PL was collected using a high-resolution monochromator and hybrid photomultiplier detector assembly (PMA Hybrid 40, PicoQuant GmbH). Perovskite films were prepared on flat substrate as previously reported,¹⁶ with Spiro-OMeTAD as hole transporter, and poly(methyl methacrylate) (PMMA) used as an insulating organic layer to replace the hole transporter.

Meso-Superstructured Solar Cells (MSSCs) Preparation. The device manufacturing was conducted according to a previously published method.¹⁵ Concisely, the devices were prepared on patterned semitransparent fluorine-doped tin oxide (FTO). A compact layer of 70 nm thick TiO_2 was deposited via spray pyrolysis at 275 °C from a precursor solution of titanium

diisopropoxide bis(acetylacetone) diluted with anhydrous ethanol at a volume ratio of 1:10. The substrate was sintered at 500 °C for 45 min and left to cool to room temperature. The samples were then submerged in a 15 mM aqueous TiCl_4 bath at 70 °C for 1 h, followed by rinsing with deionized water and resintering at 500 °C for 45 min. The next layer of mesoporous Al_2O_3 was deposited by spin-coating a colloidal dispersion of Al_2O_3 nanoparticles in isopropanol (Sigma-Aldrich) diluted with isopropanol at a volume ratio of 1:2, at 2000 rpm (ramp: 2000 rpm/s) for 60 s, followed by drying at 150 °C for 30 min.

The perovskite precursor (40 wt % of methylammonium iodide ($\text{CH}_3\text{NH}_3\text{I}$) and lead(II) chloride (PbCl_2), 3:1 molar ratio in dimethylformamide) was spin-coated at 2500 rpm (ramp: 2500 rpm/s) for 60 s. We modified the procedure slightly at this point by utilizing “hot substrate spin coating”; i.e., the perovskite precursor and the samples are preheated to 70 °C. The substrate is transferred quickly to the spin-coater; the precursor solution is deposited immediately afterward, and the spin coating is started. This procedure has yielded consistently thicker capping layer of perovskites and higher short-circuit currents.

The perovskite forms after subsequent annealing at 100 °C for 45 min. Then, the hot samples were directly immersed in an iodopentafluorobenzene (IPFB, Chemical Abstract Services Number 827-15-6) solution for a few minutes and thereafter dried under a nitrogen flow.

Subsequently, the hole transporting material was deposited by spin-coating (at 2000 rpm, ramp: 2000 rpm/s for 60 s) 80 mM 2,2',7,7'-tetrakis(*N,N*-dimethoxyphenylamine)9,9'-spiro-bifluorene (Spiro-OMeTAD) in chlorobenzene with added 80 mol% *tert*-butylpyridine (tBP) and 30 mol% of lithium bis(trifluoromethanesulfonyl)imide (Li-TFSI). Finally, 150 nm thick silver electrodes were evaporated onto the devices through a shadow mask.

Solar Cells Characterization. For measuring the performance of the solar cells, simulated sunlight was generated with a class AAB ABET solar simulator calibrated to give simulated AM 1.5, of 106.5 mW cm⁻² equivalent irradiance, using an NREL-calibrated KG5 filtered silicon reference cell. The mismatch factor was calculated to be 1.065 between 300 and 900 nm, which is beyond the operating range of both the KG5 filtered silicon reference cell and the perovskite test cells.⁴³ The current–voltage curves were recorded with a sourcemeter (Keithley 2400) scanning at 0.15 V/s from 1.4 to 0 V. The solar cells were masked with a metal aperture defining the active area (0.08 cm²) of the solar cells. All devices were stored in air and in dark for 12 h before testing.

Ultrafast Transient Absorption Measurements. The laser train pulses comes from a Ti-Sapphire source, with a maximum output energy of about 800 μJ , 1 kHz repetition rate, central wavelength of 780 nm, and pulse duration of about 180 fs. The fundamental train is divided into two branches: the pump and the probe beams. The pump pulse has been tuned at 500 nm via a noncollinear optical parametric amplification, leading a pulse duration around 100 fs.⁴⁷ Pump pulses, delayed with respect to the probe with a motorized optical stage, are focused in a 200 μm diameter spot. The probe beam is obtained in the visible and near IR region by generating white light supercontinuum in a 3 mm thick sapphire plate. Chirp-free transient transmission spectra are collected by using a fast optical multichannel analyzer with a dechirping algorithm. The measured quantity is the normalized transmission change: $\Delta T/T$. Excitation energy has been held around 20 nJ in order to

prevent saturation of the optical transitions. The system has sensitivity of the order of 10^{-4} and a time resolution of 150 fs. All measurements are performed in vacuum to prevent any oxygen effect and/or sample degradation.

Nanosecond–Millisecond Transient Absorption Measurements. The nanosecond transient absorption technique is based on a standard pump–probe flash photolysis setup, in which the sample is first excited by a strong nanosecond laser pulse (pump), and the time evolution of the differential absorption changes induced by the pump is monitored by a second, delayed weak probe pulse electronically delayed flash from a lamp. A laser pulse generated by an OPO laser (Opolette-model) tunable from 350 to 2500 nm of 5 ns pulse duration is used as pump, while the broad and weaker light from a xenon lamp is used as a probe. The transmitted probe is then spectrally filtered by a monochromator and detected. Two detectors are used: a cooled CCD camera, which detects the whole probe spectrum from 400 to 800 nm, or a series of photomultipliers, enabling the collection of the single-wavelength kinetics with higher sensitivity and in a broader spectral range from 400 nm to 2.5 μ m. The delay is electronically controlled by synchronizing the shutter on the probe line with the laser pump and with the detector. The spectrometer monitors the intensity (I_t) of the transmitted probe light passing through the sample during, before, and after the intense laser pulse. From the transmission change, the variation in the absorption is thus derived:

$$\Delta OD(t, \lambda) = -\log[I_t(\tau, \lambda)/I_{\text{probe}}]$$

where I_{probe} is the transmitted probe intensity without pump excitation and I_t is the transmitted probe upon pump excitation. The system has sensitivity of the order of 10^{-3} and a time resolution of 5 ns.

Photovoltage and Photocurrent Decay Measurements and Devices Preparation. Photovoltage and photocurrent decay measurements were performed by a similar method to O'Regan and co-workers, as described elsewhere.^{50,53}

Perovskite-sensitized solar cells (PSSCs) were prepared similarly to the MSSCs, replacing the mesoporous Al_2O_3 layer with 1.5 μm thick mesoporous TiO_2 , which was deposited by screen-printing a commercial paste (Dyesol 18NR-T). The TiO_2 films were slowly heated to 500 °C and were sintered for 30 min in air. Once cooled, the samples were immersed into a 15 mM TiCl_4 aqueous solution for 45 min at 70 °C and then sintered at 500 °C for 45 min. After cooling to 70 °C, perovskite precursor, 10 wt % of methylammonium iodide ($\text{CH}_3\text{NH}_3\text{I}$) and lead(II) chloride (PbCl_2), 3:1 molar ratio, in dimethylformamide was deposited by spin-coating at 2000 rpm for 60 s. The perovskite forms after subsequent annealing at 100 °C for 45 min. Then the samples were directly immersed in the IPFB solution for a few minutes. Upon drying the IPFB in nitrogen flow, the hole transporting material was deposited by spin-coating (1000 rpm, 60 s) 80 mM Spiro-OMeTAD in chlorobenzene with added 80 mol % tBP and 30 mol % of Li-TFSI. Finally, 150 nm thick silver electrodes were evaporated onto the devices through a shadow mask.

Photoinduced Absorption Spectroscopy. Films for CW-photoinduced absorption (PIA) were excited with an Ar-ion laser tuned to 514.5 nm (maximal intensity of 50 mW cm^{-2}) and chopped at 23 Hz. A continuous white light probe produced by a halogen bulb (\sim 1 sun intensity) was passed through the sample and detected using a monochromator (Spectra Pro 2300i, Acton Research Corp.) coupled to diodes

for detection in the visible (PDA10A, Thorlabs) and in the NIR (ID-441-C, Acton Research Corp.). Data were acquired using a lock-in amplifier (SR830, Stanford Research Systems) locked to the light modulation frequency and a NI USB-6008 (National Instruments) acquisition card. A customized Labview (National Instruments) program provided an automated interface to control hardware and record spectra.

■ ASSOCIATED CONTENT

§ Supporting Information

X-ray scattering patterns and light absorptance spectra of perovskite films coated upon mesoporous Al_2O_3 scaffolds, with and without IPFB, device performance variations with substrate temperature for perovskite deposition, device performance variations with and without IPFB, device performance parameters for record batch with IPFB treatment, ultrafast transient absorption spectra of perovskite film with Spiro-OMeTAD in visible and near-IR region with and without IPFB, quasi-steady-state photoinduced absorption (PIA) of perovskite film with and without Spiro-OMeTAD, device performance parameters for PSSCs 1.5 μm thick mesoporous TiO_2 with and without IPFB, photovoltage and photocurrent decay measurement for DSSCs with and without IPFB, photocurrent decay measurement for PSSCs with and without IPFB, photovoltage decay measurement for MSSCs with and without IPFB, device performance parameters for DSSCs with and without IPFB, device performance parameters for MSSCs with and without IPFB, device performance parameters for MSSCs with different perfluorocarbon treatments, device performance parameters for MSSCs with iodine-free perfluorocarbon treatment, stabilized steady-state power output with and without IPFB treatment, stabilized steady-state power output for record device with IPFB treatment, external quantum efficiency (EQE) spectra of perovskite MSSCs with and without IPFB treatment, solid-state ^{13}C and ^{19}F NMR spectra for IPFB as a liquid and when adsorbed onto the perovskite surface tetra-*n*-butylammonium iodide and alumina. This material is available free of charge via the Internet at <http://pubs.acs.org>.

■ AUTHOR INFORMATION

Corresponding Author

*E-mail h.snaith1@physics.ox.ac.uk (H.J.S.).

Notes

The authors declare no competing financial interest.

■ ACKNOWLEDGMENTS

This work was funded by the Engineering and Physical Sciences Research Council (EPSRC) APEX project and the European Commission, under the ERC-Stg2011 project HYPER. The research leading to these results has also received funding from the European Union Seventh Framework Programme [FP7/2007-2013] under grant agreement number 604032 of the MESO project.

■ REFERENCES

- (1) Chu, S.; Majumdar, A. *Nature* **2012**, 488, 294–303.
- (2) Butler, D. *Nature* **2008**, 454, 558–559.
- (3) Kojima, A.; Teshima, K.; Shirai, Y.; Miyasaka, T. *J. Am. Chem. Soc.* **2009**, 131, 6050–6051.
- (4) Kim, H.-S.; Lee, C.-R.; Im, J.-H.; Lee, K.-B.; Moehl, T.; Marchioro, A.; Moon, S.-J.; Humphry-Baker, R.; Yum, J.-H.; Moser, J. E. *Sci. Rep.* **2012**, 2, 591.
- (5) Lee, M. M.; Teuscher, J.; Miyasaka, T.; Murakami, T. N.; Snaith, H. J. *Science* **2012**, 338, 643–647.

- (6) Kim, H. S.; Im, S. H.; Park, N.-G. *J. Phys. Chem. C* **2014**, *118*, 5615–5625.
- (7) O'Regan, B.; Gratzel, M. *Nature* **1991**, *353*, 737–740.
- (8) Daeneke, T.; Kwon, T.-H.; Holmes, A. B.; Duffy, N. W.; Bach, U.; Spiccia, L. *Nat. Chem.* **2011**, *3*, 211–215.
- (9) Burschka, J.; Pellet, N.; Moon, S.-J.; Humphrey-Baker, R.; Gao, P.; Nazeeruddin, M. K.; Grätzel, M. *Nature* **2013**, *499*, 316–319.
- (10) Kim, H.-S.; Mora-Sero, I.; Gonzalez-Pedro, V.; Fabregat-Santiago, F.; Juarez-Perez, E. J.; Park, N.-G.; Bisquert, J. *Nat. Commun.* **2013**, *4*, 2242.
- (11) Xing, G.; Mathews, N.; Sun, S.; Lim, S. S.; Lam, Y. M.; Grätzel, M.; Mhaisalkar, S.; Sum, T. C. *Science* **2013**, *342*, 344–347.
- (12) Xing, G.; Mathews, N.; Lim, S. S.; Yantara, N.; Liu, X.; Sabba, D.; Grätzel, M.; Mhaisalkar, S.; Sum, T. C. *Nat. Mater.* **2014**, *13*, 476–480.
- (13) Stranks, S. D.; Eperon, G. E.; Grancini, G.; Menelaou, C.; Alcocer, M. J.; Leijtens, T.; Herz, L. M.; Petrozza, A.; Snaith, H. J. *Science* **2013**, *342*, 341–344.
- (14) Edri, E.; Kirmayer, S.; Kulbak, M.; Hodes, G.; Cahen, D. *J. Phys. Chem. Lett.* **2014**, *5*, 429–433.
- (15) Ball, J. M.; Lee, M. M.; Hey, A.; Snaith, H. *Energy Environ. Sci.* **2013**, *6*, 1739–1743.
- (16) Eperon, E. G.; Burlakov, M. V.; Docampo, P.; Goriely, A.; Snaith, J. H. *Adv. Funct. Mater.* **2013**, *24*, 151–157.
- (17) Liu, M.; Johnston, B. M.; Snaith, J. H. *Nature* **2013**, *501*, 395–398.
- (18) Edri, E.; Kirmayer, S.; Henning, A.; Mukhopadhyay, S.; Gartsman, K.; Rosenwaks, Y.; Hodes, G.; Cahen, D. *Nano Lett.* **2014**, *14*, 1000–1004.
- (19) Juárez-Pérez, E. J.; Wussler, M.; Fabregat-Santiago, F.; Lakus-Wollny, K.; Mankel, E.; Mayer, T.; Jaegermann, W.; Mora-Sero, I. J. *Phys. Chem. Lett.* **2014**, *5*, 680–685.
- (20) Chen, Q.; Zhou, H.; Hong, Z.; Luo, S.; Duan, H.-S.; Wang, H.-H.; Liu, Y.; Li, G.; Yang, Y. *J. Am. Chem. Soc.* **2013**, *136*, 622–625.
- (21) Gonzalez-Pedro, V.; Juárez-Pérez, E. J.; Arsyad, W. S.; Barea, E. M.; Fabregat-Santiago, F.; Mora-Sero, I.; Bisquert, J. *Nano Lett.* **2014**, *14*, 888–893.
- (22) Aberle, A. G. *Prog. Photovoltaics* **2000**, *8*, 473–487.
- (23) Lindblad, R.; Bi, D.; Park, B.-w.; Oscarsson, J.; Gorgoi, M.; Siegbahn, H.; Odelius, M.; Johansson, E. M.; Rensmo, H. *J. Phys. Chem. Lett.* **2014**, *5*, 648–653.
- (24) Kitazawa, N.; Watanabe, Y.; Nakamura, Y. *J. Mater. Sci.* **2002**, *37*, 3585–3587.
- (25) Choi, J. J.; Yang, X.; Norman, Z. M.; Billinge, S. J.; Owen, J. S. *Nano Lett.* **2013**, *14*, 127–133.
- (26) Baikie, T.; Fang, Y.; Kadro, J. M.; Schreyer, M.; Wei, F.; Mhaisalkar, S. G.; Graetzel, M.; White, T. J. *J. Mater. Chem. A* **2013**, *1*, S628–S641.
- (27) Abate, A.; Biella, S.; Cavallo, G.; Meyer, F.; Neukirch, H.; Metrangolo, P.; Pilati, T.; Resnati, G.; Terraneo, G. *J. Fluorine Chem.* **2009**, *130*, 1171–1177.
- (28) Tasker, P. *J. Phys. C: Solid State Phys.* **1979**, *12*, 4977–4984.
- (29) Legon, A. *Chem. Soc. Rev.* **1993**, *22*, 153–163.
- (30) Flensburg, C.; Larsen, S.; Stewart, R. F. *J. Phys. Chem.* **1995**, *99*, 10130–10141.
- (31) Roe, A. L.; Hayes, K. F.; Chisholm-Brause, C.; Brown, G. E., Jr.; Parks, G. A.; Hodgson, K. O.; Leckie, J. O. *Langmuir* **1991**, *7*, 367–373.
- (32) Itzhaik, Y.; Niitsoo, O.; Page, M.; Hodes, G. *J. Phys. Chem. C* **2009**, *113*, 4254–4256.
- (33) Wilson, A. J. *Nat. Chem.* **2011**, *3*, 193–194.
- (34) Slough, W. *J. Chem. Soc., Faraday Trans.* **1959**, *55*, 1030–1035.
- (35) Metrangolo, P.; Resnati, G. *Nat. Chem.* **2012**, *4*, 437–438.
- (36) Meazza, L.; Foster, J. A.; Fucke, K.; Metrangolo, P.; Resnati, G.; Steed, J. W. *Nat. Chem.* **2012**, *5*, 42–47.
- (37) Nguyen, H. L.; Horton, P. N.; Hursthouse, M. B.; Legon, A. C.; Bruce, D. W. *J. Am. Chem. Soc.* **2004**, *126*, 16–17.
- (38) Huber, S. M.; Scanlon, J.; Jimenez-Izal, E.; Ugalde, J. M.; Infante, I. *Phys. Chem. Chem. Phys.* **2013**, *15*, 10350–10357.
- (39) Abate, A.; Martí-Rujas, J.; Metrangolo, P.; Pilati, T.; Resnati, G.; Terraneo, G. *Cryst. Growth Des.* **2011**, *11*, 4220–4226.
- (40) Zhang, Y.; Ji, B.; Tian, A.; Wang, W. *J. Chem. Phys.* **2012**, *136*, 141101.
- (41) Viger-Gravel, J.; Leclerc, S.; Korobkov, I.; Bryce, D. L. *CrystEngComm* **2013**, *15*, 3168–3177.
- (42) Budarin, V. L.; Clark, J. H.; Hale, S. E.; Tavener, S. J.; Mueller, K. T.; Washton, N. M. *Langmuir* **2007**, *23*, 5412–5318.
- (43) Snaith, H. J. *Energy Environ. Sci.* **2012**, *5*, 6513–6520.
- (44) Kumar, A.; Sista, S.; Yang, Y. *J. Appl. Phys.* **2009**, *105*, 094512.
- (45) Wagenpfahl, A.; Rauh, D.; Binder, M.; Deibel, C.; Dyakonov, V. *Phys. Rev. B* **2010**, *82*, 115306.
- (46) Canesi, E. V.; Binda, M.; Abate, A.; Guarnera, S.; Moretti, L.; D'Innocenzo, V.; Kumar, R. S. S.; Bertarelli, C.; Abrusci, A.; Snaith, H. *Energy Environ. Sci.* **2012**, *5*, 9068–9076.
- (47) Cabanillas-Gonzalez, J.; Grancini, G.; Lanzani, G. *Adv. Mater.* **2011**, *23*, 5468–5485.
- (48) Marchioro, A.; Teuscher, J.; Friedrich, D.; Kunst, M.; van de Krol, R.; Moehl, T.; Grätzel, M.; Moser, J.-E. *Nat. Photonics* **2014**, *8*, 250–255.
- (49) Abate, A.; Hollman, D. J.; Teuscher, J.; Pathak, S.; Avolio, R.; D'Errico, G.; Vitiello, G.; Fantacci, S.; Snaith, H. *J. Am. Chem. Soc.* **2013**, *135*, 13538–13548.
- (50) Barnes, P. R.; Miettunen, K.; Li, X.; Anderson, A. Y.; Bessho, T.; Gratzel, M.; O'Regan, B. C. *Adv. Mater.* **2013**, *25*, 1881–1922.
- (51) Zhao, Y.; Nardes, A. M.; Zhu, K. *J. Phys. Chem. Lett.* **2014**, *5*, 490–494.
- (52) Fry, R. A.; Tsomaia, N.; Pantano, C. G.; Mueller, K. T. *J. Am. Chem. Soc.* **2003**, *125*, 2378–2379.
- (53) O'Regan, B.; Xiaoe, L.; Ghaddar, T. *Energy Environ. Sci.* **2012**, *5*, 7203–7215.